Princeton Plasma Physics Laboratory

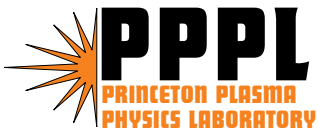## Global Hybrid Simulations of Energetic Particle Effects on the n=1 Mode in Tokamaks: Internal Kink and Fishbone Instability

G.Y. Fu, W. Park, H.R. Strauss, J. Breslau,
J. Chen, S. Jardin, and L.E. Sugiyama

August 2005

PPPL Report Disclaimers

Full Legal Disclaimer

Trademark Disclaimer

PPPL Report Availability

Global hybrid simulations of energetic particle effects on the n=1 mode in tokamaks: internal kink and fishbone instability

G. Y. Fu[a], W. Park[a], H. R. Strauss[b], J. Breslau[a], J. Chen[a], S. Jardin[a] and L.E. Sugiyama[c]

[a]*Princeton Plasma Physics Laboratory, Princeton, New Jersey 08543*

[b]*New York University, New York, NY*

[c]*MIT, Cambridge, MA*

(August 10, 2005)

Abstract

Global hybrid simulations of energetic particle effects on the n=1 internal kink mode have been carried out for tokamaks. For the Internationa Thermonuclear Experimental Reactor (ITER) [ITER Physics Basis Editors et al, Nucl. Fusion 39, 2137 (1999).], it is shown that alpha particle effects are stabilizing for the internal kink mode. However, the elongation of ITER reduces the stabilization effects significantly. Nonlinear simulations of the precessional drift fishbone instability for circular tokamak plasmas show that the mode saturates due to flattening of the particle distribution function near the resonance region. The mode frequency chirps down rapidly as the flattening region expands radially outward. Fluid nonlinearity reduces the saturation level.

I. INTRODUCTION

As we approach burning plasma experiments such as the Internationa Thermonuclear Experimental Reactor (ITER) [1], the physics of energetic particles is an area of increasing importance. A key issue is how energetic alpha particles would affect the bulk plasmas and

1

whether alpha-driven Magnetohydrodynamics (MHD) instabilities will induce large alpha particle transport and associated losses. To answer this question, we need self-consistent numerical simulations which can predict alpha particle-driven instabilities in the new parameter regimes of burning plasmas. Towards this end, we have developed a particle/MHD hybrid code, M3D, to study the physics of energetic particle-driven instabilities in present and future fusion devices. In this work, we focus on energetic particle effects on the n=1 kink mode (where n is the toroidal mode number), namely, alpha particle stabilization of the internal kink mode in ITER and the nonlinear dynamics of energetic particle-driven fishbone instability in tokamaks.

The M3D code contains multiple levels of physics models including resistive MHD, two fluids [3], and particle/MHD hybrid. In the present work, the particle/MHD hybrid model is used. In this model, the plasma is divided into two parts: the bulk plasma (thermal electrons and ions) and the energetic particles. The bulk plasma is treated as a single fluid whereas the energetic particles are treated either as drift-kinetic or gyrokinetic particles. The details of the model are described in the next section.

The original version of the M3D hybrid code has been applied to study nonlinear saturation of energetic particle-driven Toroidal Alfvén Eigenmodes [4], stabilization of the internal kink mode and the excitation of the fishbone instability [2]. Recently, we have extended the hybrid level of M3D code to general 3D meshes by using linear finite elements in the poloidal planes and finite differences in the toroidal direction [5]. These new capabilities have enabled us to study energetic particle-driven modes in many types of fusion devices including shaped tokamaks such as ITER, spherical tokamaks [6] and stellarators [7]. In this work, we present results on alpha particle stabilization of internal kink mode in ITER and on the nonlinear evolution of the fishbone instability.

The energetic particle stabilization of the internal kink mode has been studied extensively. The stabilization comes from conservation of the third invariant when the energetic particle precession frequency is much larger than the MHD growth rate [8,9]. Most previous work [10–13] used analytic methods valid for large aspect ratio circular tokamaks. General shaped

tokamak equilibria have been considered in a few studies only [14–16]. In this work, we consider alpha particle stabilization of the internal kink in ITER. In particular, we study shaping effects on the alpha stabilization. We find that the elongation of ITER significantly reduces the stabilization compared to that of an equivalent tokamak with circular cross section. In contrast, Wu, Cheng and White [15] found that elongation enhances alpha stabilization. We believe the discrepancy arises because they ony considered the effect of shaping on alpha particle's precessional drift frequency. More details are discussed in Sec. IV.

On the second topic of this paper, we have carried out extensive nonlinear simulations of the fishbone instability driven by energetic particles in tokamaks. The fishbone is an $n = 1$ internal mode with dominant poloidal mode number $m = 1$ which is resonantly destabilized by energetic trapped particles. It was first discovered [17] in the Princeton tokamak Divertor Experiments (PDX) in 1980. The name came from its characteristic shape of the Mirnov magnetic signal. Since then, the instability has been observed in many tokamaks and stellarators. Extensive theoretical work has been done over the years. There were two early competing theories to explain the experimental observations. Chen et $al.$ [18] proposed that the mode is destabilized by energetic trapped ions via precessional drift resonance($\omega = \omega_d$) and that the mode is intrinsically an energetic particle mode. Coppi et $al.$ [19] proposed that the mode is MHD-like with a frequency on the order of the thermal ion's diamagnetic drift frequency ($\omega = \omega_{\star i}$). More recently, the possibility of a fishbone instability driven by the bounce resonance has also been proposed [20]. Finally, there is the possibility of the fishbone being driven by circulating particles [21]. In this work, we focus on the precessional drift branch due to its interesting nonlinear behavior.

Compared to linear theory, the nonlinear theory of the fishbone is less mature. Early work used phenomelogical predator-prey models [18,22,23] to explain the mode saturation and bursting due to resonant particle loss. More recently, Candy et $al.$ [24] simulated a full cycle of fishbone oscillations by using a simplified hybrid model where a fixed internal kink mode structure was used. The fluid nonlinearity was neglected and the mode saturation was due

entirely to the particle nonlinearity. On the other hand, Odblom *et al.* [25] investigated the fluid nonlinearity of the fishbone instability while neglecting the particle nonlinearity. They found that the fluid nonlinearity enhances the initial growth rate near marginal stability. In this work, we use a fully self-consistent model which includes both particle and fluid nonlinearities. The mode structure is self-consistently determined both in the linear and nonlinear regime including energetic particle effects. We find that the nonlinear dynamics is mainly determined by the particle nonlinearity. The mode saturates due to flattening of the particle distribution in the resonance region. The mode frequency chirps down significantly as the width of flattening region increases. The fluid nonlinearity is found to reduce the saturation level.

The paper is organized as follows. Sec II. describes the hybrid model used in this work. Sec. III describes the benchmarking of the M3D hybrid code. Sec. IV describes the results for alpha particle stabilization of the internal kink mode in ITER. Sec. V describes the results of nonlinear simulations of the fishbone instability. Finally, conclusions are given in Sec. VI.

II. PARTICLE/MHD HYBRID MODEL

In this work, we use a particle/MHD hybrid model to describe the interaction of energetic particles and MHD waves. In the model [2], the plasma is divided into two parts: the thermal component and the energetic particle component. The thermal ions and electrons are treated as a single fluid. The energetic species is treated as drift-kinetic particles or gyrokinetic particles. The energetic particle effects enter through the particle stress tensor $\mathbf{P}_h$ in the momentum equation:

$$\rho \frac{d\mathbf{v}}{dt} = -\nabla P - \nabla \cdot \mathbf{P}_h + \mathbf{J} \times \mathbf{B} . \tag{1}$$

Equation (1) is closed by the Maxwell equations

$$\mathbf{J} = \nabla \times \mathbf{B}, \qquad \frac{\partial \mathbf{B}}{\partial t} = -\nabla \times \mathbf{E} , \tag{2}$$

4

Ohm's law

$$\mathbf{E} + \mathbf{v} \times \mathbf{B} = \eta \mathbf{J} \ , \tag{3}$$

continuity equation for plasma mass density

$$d\rho/dt = -\rho \nabla \cdot \mathbf{v}. \tag{4}$$

and the pressure equation for thermal species

$$dP/dt = -\gamma P \nabla \cdot \mathbf{v}. \tag{5}$$

The particle stress tensor is taken to be in the Chew-Goldberger-Low (CGL) form

$$\mathbf{P}_h = P_\perp \mathbf{I} + (P_\parallel - P_\perp)\mathbf{bb} \ , \tag{6}$$

where the parallel and perpendicular pressure is calculated from the particle distribution function F in the gyrocenter coordinates $(\mathbf{X}, v_\parallel, \mu)$:

$$
\begin{aligned}
P_\parallel(\mathbf{x}) &= \int M v_\parallel^2 \delta(\mathbf{x} - \mathbf{X} - \rho_\mathbf{h}) F(\mathbf{X}, v_\parallel, \mu) d^3\mathbf{X} dv_\parallel d\mu d\theta \\
P_\perp(\mathbf{x}) &= \int \frac{1}{2} M v_\perp^2 \delta(\mathbf{x} - \mathbf{X} - \rho_\mathbf{h}) F(\mathbf{X}, v_\parallel, \mu) d^3\mathbf{X} dv_\parallel d\mu d\theta
\end{aligned}
\tag{7}
$$

where $\rho_h = \mathbf{v}_\perp \times \mathbf{b}/\Omega$ is the gyroradius vector, $(\mathbf{x}, \mathbf{v})$ is the particle physical space coordinates, μ is the magnetic moment and θ is the gyroangle.

The gyrocenter distribution F is represented by an ensemble of markers as

$$f = f(\mathbf{X}, v_\parallel, \mu) = \sum_i \delta(\mathbf{X} - \mathbf{X}_i)\delta(v_\parallel - v_{\parallel,i})\delta(\mu - \mu_i) \tag{8}$$

The marker's orbits follow from the gyrokinetic equations:

$$\frac{d\mathbf{X}}{dt} = \frac{1}{B^{\star\star}}\left[v_\parallel(\mathbf{B}^\star - \mathbf{b_0} \times (<\mathbf{E}> -\frac{1}{e}\mu\nabla(B_0 + <\delta B>)))\right] \tag{9}$$

$$m\frac{dv_\parallel}{dt} = \frac{e}{B^{\star\star}}\mathbf{B}^\star \cdot (<\mathbf{E}> -\frac{1}{e}\mu\nabla(B_0 + <\delta B>)) \tag{10}$$

Here $\mathbf{E}$ is the total electric field, $\mathbf{B}$ is the total magnetic field, $\mathbf{b_0}$ is the unit vector in the direction of the equilibrium magnetic field, and B_0 and δB are the equilibrium and

perturbed magnetic field respectively. Note that the bracket $<>$ represents gyro-average. The variables $\mathbf{B}^\star$ and $B^{\star\star}$ are given by

$$\mathbf{B}^\star = \mathbf{B_0} + <\delta\mathbf{B}> + \frac{mv_\parallel}{q}\nabla \times \mathbf{b_0}, \quad B^{\star\star} = \mathbf{B}^\star \cdot \mathbf{b_0} \qquad (11)$$

The system of coupled equations (1-11) is a complete particle/MHD hybrid model which is self-consistent, three dimensional, and nonlinear. The coupled equations are solved as an initial value problem. The δf method is used for the energetic particles. More details of the δf method and the particle part of the code are given in the appendices.

It should be noted that the gyrokinetic equations (Eq. (9)) reduce to the drift kinetic equations without gyro-average. For simplicity, all results presented here are obtained using the drift kinetic model.

Finally, we note that similar hybrid models have been used by others in the simulations of energetic particle-driven toroidal Alfvén eigenmodes [26,27].

III. BENCHMARKING OF THE M3D HYBRID CODE

The hybrid code M3D has been benchmarked extensively for both single particle orbits and collective effects of energetic particles on internal kink mode, fishbone instability and toroidal Alfvén eigenmodes. In particular, the new version of the code with unstructured mesh has been benchmarked against the original Fourier version of M3D [2]. For single particle orbits in tokamak equilibria, the particle energy and toroidal angular momentum are well conserved. The calculated linear TAE mode frequencies and growth rates agree well with those of the perturbative kinetic MHD linear eigenvalue code NOVA-K [28]. For a tokamak equilibrium, the results of M3D agree well with the NOVA2 [14] code for an n=1 internal kink mode and fishbone mode. Figure 1 compares the n=1 mode frequency and growth rates of NOVA2 and M3D as a function of the energetic particle beta at the center of plasma. We note that the agreement is quite good. The small difference could be caused by differences in the models. The NOVA2 code is a non-perturbative version of the NOVA-K code which

only includes the trapped particle response of the precessional resonance in the limit of zero orbit width. The M3D code includes all wave particle resonances for both trapped and passing particles and full drift orbits. Since the trapped particle precessional resonance is the dominant response of energetic particles, we expect the differences in the models are not important, as confirmed by Fig. 1. The results are obtained for a circular tokamak with aspect ratio $R/a = 2.763$, total central beta $\beta_{total}(0) = 8.0\%$. The plasma density profile is uniform and the bulk plasma pressure profile is given by $P(\Psi) = P(0) \exp(-\Psi/0.25)$ where Ψ is the normalized poloidal flux variable with $\Psi = 0$ at the center and $\Psi = 1$ at the edge of the plasma. The safety factor profile is given by

$$q = q_0 + \Psi \left[q_1 - q_0 + (q_1' - q_1 + q_0) \frac{(1 - \Psi_s)(\Psi - 1)}{\Psi - \Psi_s} \right] \tag{12}$$

where $\Psi_s = (q_1' - q_1 + q_0)/(q_0' + q_1' - 2q_1 + 2q_0)$, $q_0 = 0.6$, $q_1 = 2.5$, $q_0' = 0.78$ and $q_1' = 5.0$. An isotropic slowing-down distribution is used for energetic particles and is given by

$$f = \frac{cH(v_0 - v)}{v^3 + v_c^3} \exp(- < \Psi > /0.25) \tag{13}$$

where v_0 is the maximum particle speed, $v_c = 0.58 v_0$ is the critical velocity, c is a normalization factor, and $< \Psi >$ is Ψ averaged over the particle orbit. Since the toroidal angular momentum $P_\phi = e\Psi + Mv_\parallel R B_\phi/B$ is conserved, we can write

$$< \Psi > = P_\phi/e - \frac{M}{e} < v_\parallel R \frac{B_\phi}{B} > \tag{14}$$

where e is the particle charge, M the mass. For simplicity, we make use of the approximations

$$< v_\parallel R \frac{B_\phi}{B} > \approx 0 \tag{15}$$

for trapped particles and

$$< v_\parallel R \frac{B_\phi}{B} > \approx sign(v_\parallel)\sqrt{1 - \mu B_0/E} R_0 \tag{16}$$

for passing particles, with B_0 and R_0 being the magnetic field strength and major radius at the magnetic axis. Finally, the normalized particle gyroradius and speed is given by $\rho_h = v_0/(\Omega_{ch} a) = 0.0125$ and $v_0/v_A = 4$ where $\Omega_{ch} = eB_0/(Mc)$ is the energetic particle's cyclotron frequency.

IV. ALPHA PARTICLE STABILIZATION OF INTERNAL KINK MODE IN ITER

We now consider the effects of fusion alpha particles on the stability of the internal kink mode in burning plasmas. Specifically, we consider parameters and profiles of ITER. It is well known that energetic particles such as high energy alpha particles have a significant stabilization effect on the internal kink mode. There have been many previous studies related to this physics. However, most of the previous work assumed large aspect ratio and circular flux surfaces. Here, we apply the M3D hybrid code, which can treat arbitrary aspect ratio and shaped plasma cross sections. We find that cross section elongation is an important effect for the alpha particle stabilization of the internal kink.

The alpha particle stabilization of the internal kink can be described in the limit of small alpha particle beta as follows:

$$\frac{\gamma}{\omega_A} = \frac{\gamma_{MHD}}{\omega_A} - \beta_\alpha(0)\delta W_\alpha , \tag{17}$$

here ω_A is the shear Alfvén frequency, γ is the net growth rate, γ_{MHD} is the MHD growth rate including alpha's pressure effects, $\beta_\alpha(0)$ is the central alpha beta, and δW_α is an order of unity numerical factor which represents the stabilizing effects of alpha particle's non-adiabatic response. In the limit of large aspect ratio, circular geometry and $1 - q(0) << 1$, δW_α can be written as [13]:

$$\delta W_\alpha = -\frac{\sqrt{3}\pi}{8s_1}\sqrt{\frac{R}{r}} \int_0^{r_1} rdr[(0.6 + 3.2(1 - q - 0.5s))(\frac{r}{r_1})^{1.5}\frac{d\hat{p}_\alpha}{dr}] \tag{18}$$

where $r = r_1$ is the minor radius at which $q(r_1) = 1.0$, s_1 is the magnetic shear at $r = r_1$, and $\hat{p}_\alpha$ is the alpha pressure normalized to unity at the center. This analytic result agrees well with our numerical results for a model tokamak equilibrium with circular flux surfaces.

We now consider the case of ITER. The main parameters and profiles, obtained from a TRANSP simulation [29], are as follows: $B = 5.05T$, $R = 620cm$, $a = 200cm$, electron density $n_e(0) = 1.0^{14}cm^{-3}$, $T_i(0) = 19kev$, $T_e(0) = 23kev$, central total beta $\beta(0) = 6.5\%$,

$\beta_\alpha(0) = 1\%$, $q(0) \sim 0.9$, $q(a) = 3.83$. The alpha particle distribution is a slowing-down function given by Eq. (13). Using these parameters and profiles, linear simulations have been carried out to determine the alpha particle stabilization effects. Figure 2 shows the n=1 internal kink eigenmode structure with (right) and without (left) alpha particles. The MHD growth rate $\gamma_{MHD}/\omega_A = 0.0070$ is reduced to $\gamma/\omega_A = 0.0039$ with alpha particles, which corresponds to $\delta W_\alpha = 0.31$. However, the simple analytic estimate in Eq. 18 gives $\delta W_\alpha = 0.82$ which is much larger. We have shown analytically and numerically that this discrepancy is mainly due to the elongation of the ITER plasma shape. To illustrate the importance of this effect, Fig. 3 shows δW_α as a function of elongation at zero triangularity while all other parameters and profiles are fixed. We observe that the stabilization effects of alpha particles decreases as elongation increases. At the full ITER shape (elongation=1.8), alpha particle stabilization is reduced by a factor of 2.5 as compared to the circular shape case. This result shows that the elongation of plasma shape is an important factor for the alpha particle stabilization of the internal kink mode and it must be taken into account for realistic modeling of the internal kink stability and sawteeth in ITER.

It should be pointed out that our results of shaping effects are opposite to that found by Wu, Cheng and White. They found that shaping (mainly elongation) enhances the alpha particle stabilizing. The results were obtained from an analytic dispersion relation which showed δW_k is proportional to a weighted average of $\omega_{\star\alpha}/\omega_{d\alpha}$. In their work, elongation effects are retained only in the alpha precessional drift frequency $\omega_{d\alpha}$. The alpha's diamagnetic drift frequency $\omega_{\star\alpha}$ was held fixed. Since $\omega_{d\alpha}$ in proportional to $1/\kappa$ to lowest order (where κ is elongation), this effect of elongation was found to enhance the alpha particle stabilization. However, it can be shown that $\omega_{\star\alpha}$ is also proportional to $1/\kappa$ for fixed alpha pressure profile. Thus, the dependence of $\omega_{\star\alpha}$ on elongation nearly cancels the that of $\omega_{d\alpha}$. We find that our results of elongation effects can be explained in part by a higher order κ dependence of $\omega_{d\alpha}$ and by a κ dependence of the inertial term in the fishbone dispersion relation. An analytic derivation of this elongation effect will be reported elsewhere.

V. FISHBONE INSTABILITY

The fishbone instability was first discovered in the PDX tokamak. The name "fishbone" came from the characteristic shape of the magnetic signal from the Mirnov coils. It is basically an $(n,m) = (1,1)$ internal kink mode destabilized by energetic trapped particles via precessional resonance. Here we use the M3D hybrid code to study the excitation and nonlinear evolution of the fishbone instability driven by energetic particles. In particular, we investigate the nonlinear dynamics of the instability self-consistently.

We start with linear simulations. We consider a sequence of circular tokamak equilibria with increasing energetic particle pressure. The plasma parameters and profiles are the same as in Sec. III except the q profile is specified by $q_0 = 0.9$, $q_1 = 2.5$, $q_0' = 0.78$ and $q_1' = 5.0$. The energetic particle distribution is an isotropic slowing-down one given by Eq. (13) with $\rho_h/a = 0.05$ and $v_0/v_A = 1$. Figure 4 plots the fishbone growth rate and mode frequency versus energetic particle beta $\beta_h(0)$ from three cases: A) $\beta_h(0) = 2.6\%$, B) $\beta_h(0) = 4.3\%$, and C) $\beta_h(0) = 5.7\%$. The plasma thermal beta is very small, with $\beta_h/\beta_{total} \sim 0.9$ for all these cases. Figure 5 shows the velocity stream function U and the non-adiabatic part of perturbed energetic particle pressure $\delta P_\parallel$ and $\delta P_\perp$ of the linear eigenmode for case B. We observe that the eigenmode structure is mainly a $(1,1)$ mode as expected. We also observe in Fig. 4 that the growth rate increases approximately linearly as a function of $\beta_h(0)$ while the mode frequency varies slightly about $\omega \sim 0.04$. This frequency is comparable to the nominal energetic particle precessional frequency $\omega_d/\omega_A \sim \frac{1}{2} k_\theta \rho_h v_h/v_A \sim 0.05$. These results are consistent with analytic results for the fishbone instability.

We now turn to nonlinear simulation results. We first focus on the particle nonlinearity by imposing a linear MHD response from the thermal species. Figure 6 shows the nonlinear evolution of U_{cos} (the $cos\phi$ component of U) for case A, B and C. Figure 7 shows the corresponding evolution of $ln(|U|)$ where $|U| = \sqrt{U_{cos}^2 + U_{sin}^2}$ is the amplitude of U. We observe that the mode first grows linearly (seen more clearly in Fig. 7) and then begins to saturate after a few oscillations. The initial saturation amplitude scales as $U_{amp} \sim \gamma^2$ as

shown in Fig. 8. It is interesting to note that after the initial saturation, the mode amplitude can oscillate (case A with smallest growth rate), or decay slowly (case B) or decay rapidly (case C with largest linear growth rate). We also observe that the frequency of the mode chirps down significantly as the mode oscillation period increases for all these cases. This can be clearly seen in Fig. 9 where we plot the mode frequency versus time. We observe up to a factor of two reduction in mode frequency at the end the simulation runs. It should be pointed out that the calculated mode frequency is evaluated from the rate of phase change of U averaged over $\Delta t = 45$.

It is interesting to ask whether the mode structure changes significantly during the nonlinear evolution. Figure 10 plots contours of U at three times: $t = 297$ (top, linear stage), $t = 594$ (middle, inial saturation) and $t = 1578$ (late stage of nonlinear evolution), for case B. We note that the mode structure at the initial saturation is similar to the linear eigenmode, but the mode structure changes significantly at later stage of the evolution. This is actually not surprising since the mode frequency has changed by a large amount by that time.

We now investigate the physical mechanism for saturation and mode frequency chirping. Figure 11 shows the evolution of the energetic particle distribution at particle speed $v/v_A \sim$ 0.8 and pitch angle $\Lambda = \mu B_0/E \sim 1.0$. Note that the horizontal axis P_ϕ corresponds to a radial variable ranging from -0.42 at the center of plasma to 0 at the plasma edge. We observe that the distribution becomes flattened starting from $t \sim 500$ when the mode frequency begins to chirp down rapidly. Furthermore, the flattening region widens clearly from this time. Notice that the shoulder of the flattening region moves out radially in time. Since the instability is driven by df/dP_ϕ, the initial saturation is caused by the nonlinear flattening of the distribution. On the other hand, the frequency chirping can be explained by the movement of the shoulder in the distribution function. In the nonlinear evolution, we expect the mode frequency evolves according to the distribution evolution in order to maximize instability drive. In particular, we expect that the maximum drive comes from the steep gradient region just outside the shoulder region. Since the precession drift frequency

of trapped particles at fixed energy and pitch angle is smaller for larger P_ϕ (or larger radius), the mode frequency needs to decrease in time as the steep gradient region moves out radially in order to satisfy the resonant condition $\omega = \omega_d$ and tap the free energy associated with the df/dP_ϕ.

So far, we have neglected the MHD nonlinearity in the nonlinear simulations. We have also carried out simulations with both particle nonlinearity and MHD nonlinearity. Figure 12 compares fishbone amplitude evolutions with (dashed line) and without (solid line) MHD nonlinearity. The results are obtained for another fishbone case with $\omega/\omega_A = 0.078$ and $\gamma/\omega_A = 0.017$. We observe that the MHD nonlinearity reduces the initial saturation level. However, the MHD nonlinearity does not enhance the initial mode growth in contrast to the results of Odblom et al [25]. In the work of Odblom et al, the MHD nonlinear enhancement of the initial mode growth was found near marginal stability when the linear mode had a double layer radial structure around the q=1 surface. In this work, however, the linear mode has a single layer structure around the q=1 surface due to finite numerical viscosity. Results of nonlinear cases with small viscosity will be reported in future.

A word on the numerical resolution is in order here. For the simulation results presented in this work, we typically used about 61 radial zones, 7000 mesh points in a poloidal plane, and 16 toroidal zones. Up to 8 million simulation particles have been used. It is found that this numerical resolution and particle number are sufficient for the cases considered above.

Compared to the previous work of Candy *et al*. [24], the present work is more self-consistent and comprehensive. Candy *et al*. used a reduced model where the mode structures was assumed to be fixed and a simple dispersion relation for the fishbone mode was used to evolve the mode amplitude. In the work presented here, we used the full MHD equations together with energetic particle effects. The mode structure is self-consistently determined as the instability evolves nonlinearly. Our results agree with theirs in that we both find strong frequency chirping. However, our saturation levels are much higher. For example, for the case A with lowest growth rate, the saturation level in terms of plasma radial displacement is around $\xi_r/a \sim 0.24$.

Finally it should be pointed out that our results for the nonlinear fishbone is qualitatively similar to the hole-clump theory of the bump-in-tail instability by Berk et al [30]. In particular, the nonlinear frequency evolution in Fig. 10 approximately scales as $\delta f \sim \sqrt{t}$ as found analytically by their theory. Of course, quantitative agreement is not expected since our model is much more comprehensive and self-consistent.

VI. CONCLUSIONS

We have performed global hybrid simulations of the n=1 internal kink mode in the presence of energetic particles using the M3D hybrid code. For ITER parameters and profiles, the effects of alpha particles are stabilizing. However, the elongation of ITER strongly reduces the alpha stabilization effects. Thus, shaping effects should be retained in the modeling of internal kink stability and related sawteeth oscillations for ITER. On the second topic of this work, we have investigated the nonlinear dynamics of the fishbone instability in tokamaks. Our model is self-consistent, including both particle nonlinearity and MHD nonlinearity. The mode structure is self-consistently determined together with energetic particle effects. It is found that nonlinear flattening of the particle distribution function near the resonance region leads to mode saturation and strong downward frequency chirping. Thus, particle nonlinearity alone can account for the characteristic feature of experimental observations. The MHD nonlinerity reduces the initial saturation level.

out as a part of the Center for Extended MHD Modeling (CEMM) project under SciDAC. The simulations were carried out using the massively parallel supercomputer Seaborg at NERSC.

APPENDIX A: COORDINATES, FIELD VARIABLES AND DISCRETIZATION

The cylindrical coordinates (R, Z, ϕ) are used as the spacial coordinates for the M3D code. In this coordinates, the magnetic field and plasma velocity is written as

$$\mathbf{B} = \nabla\Psi \times \nabla\phi + \frac{1}{R}\nabla_\perp F + \frac{I}{\epsilon}\nabla\phi \tag{A1}$$

and

$$\mathbf{v} = \epsilon R^2 \nabla u \times \nabla\phi + \nabla_\perp \chi + R v_\phi \nabla\phi \tag{A2}$$

where

$$\nabla_\perp = \nabla R \frac{\partial}{\partial R} + \nabla Z \frac{\partial}{\partial Z} \tag{A3}$$

and $\epsilon = a/R_0$.

The time evolution equations are solved for nine independent variables Ψ, I, u, χ, v_ϕ, P, and ρ, $P_\parallel$ and $P_\perp$. Note that F is related to I from zero divergence of the magnetic field.

A linear triangle finite element method is used in the poloidal plane (i.e., in (R, Z) space) and a 4th order finite difference method is used in toroidal direction.

APPENDIX B: δF METHOD

A δf method is used to reduce particle noise in hybrid simulations. In this method, the full particle distribution is written as $f = f_0 + \delta f$ where f_0 is the equilibrium distribution and δf is the perturbed one. We define a weight $w = \delta f/g$ where g is the distribution of loaded simulation particles (or markers). The evolution equation for the weight is

$$\frac{dw}{dt} = -(\frac{f}{g} - w)\frac{1}{f_0}\frac{df_0}{dt} \tag{B1}$$

The equilibrium distribution is expressed as a function of the constants of motion:

$$f_0 = f_0(P_\phi, E, \mu) \tag{B2}$$

where P_ϕ is the toroidal angular momentum, E the energy and μ is the magnetic moment. Then

$$\frac{df_0}{dt} = \frac{dP_\phi}{dt}\frac{\partial f_0}{\partial P_\phi} + \frac{dE}{dt}\frac{\partial f_0}{\partial E} \tag{B3}$$

where

$$\frac{dE}{dt} = e\mathbf{v}_d \cdot <\mathbf{E}> + M\mu\frac{d<\delta B>}{dt} \tag{B4}$$

$$\frac{dP_\phi}{dt} = (\frac{d\mathbf{X}}{dt})_1 \cdot \nabla P_\phi + (\frac{dv_\parallel}{dt})_1\frac{\partial P_\phi}{\partial v_\parallel} \tag{B5}$$

$$(\frac{d\mathbf{X}}{dt})_1 = \frac{1}{B^{\star\star}}\left[v_\parallel(\delta\mathbf{B} - \mathbf{b_0} \times (<\delta\mathbf{E}> -\frac{1}{e}\mu\nabla<\delta B>)\right] \tag{B6}$$

$$m(\frac{dv_\parallel}{dt})_1 = \frac{e}{B^{\star\star}}\delta\mathbf{B} \cdot (<\mathbf{E}> -\frac{1}{e}\mu\nabla(B_0 + <\delta B>)) + \frac{e}{B_0^{\star\star}}\mathbf{B}^\star \cdot (<\delta\mathbf{E}> -\frac{1}{e}\mu\nabla<\delta B>) \tag{B7}$$

where the subscript 1 denotes the perturbed part. In term of particle weight, the perturbed parallel and perpendicular pressure is given by

$$\delta P_\parallel(\mathbf{x}) = \int Mv_\parallel^2\delta(\mathbf{x} - \mathbf{X} - \rho_\mathbf{h})(w + \frac{\delta B^{\star\star}}{B^{\star\star}}(\frac{f}{g} - w))B^{\star\star}gd^3\mathbf{X}dv_\parallel d\mu d\theta$$

$$\delta P_\perp(\mathbf{x}) = \int \frac{1}{2}Mv_\perp^2\delta(\mathbf{x} - \mathbf{X} - \rho_\mathbf{h})(w + \frac{\delta B^{\star\star}}{B^{\star\star}}(\frac{f}{g} - w) + \frac{\delta B}{B}\frac{f}{g})B^{\star\star}gd^3\mathbf{X}dv_\parallel d\mu d\theta \tag{B8}$$

APPENDIX C: PARTICLE CALCULATIONS WITH UNSTRUCTURED MESH

Here we briefly describe the numerical methods used in the particle part of the hybrid code. This part of code consists of three main steps: (a) particle loading; (b) particle pushing;

and (c) calculations of $P_\parallel$ and $P_\perp$. In the particle part, we use the same unstructured mesh and triangle elements as in the fluid part of the code. In order to push particles and to calculate the particle pressure, it is essential to locate which triangle cell each particle is in. To aid particle search, we use an auxiliary set of coordinates (x, y, ϕ) in addition to the cylindrical coordinates (R, Z, ϕ) for particles. This set of (x, y, ϕ) is related to the flux coordinates (s, θ, ϕ) as follows:

$$x = \sqrt{s}\cos(\theta)$$
$$y = \sqrt{s}\sin(\theta) \tag{C1}$$

where s is chosen to be the normalized toroidal flux. We carry out particle search in this coordinates because the unstructured mesh is constructed based on the flux coordinates. Once (x, y, ϕ) is known for a particle, it is quite straightforward to determine which cell it is in.

First, we consider particle loading. In general we can use any marker distribution g. For convenience, we usually load particles uniformly in $(R, Z, \phi, v_\parallel, v_\perp^2)$ space. This corresponds to a marker distribution of $g = B/B^{\star\star}$.

Second, we describe particle pushing. We use the Leap-Frog scheme to push particles according Eq. (9). To do this, we need to evaluate fields at each particle position. For any field (e.g., B), the value at the particle location can be determined by

$$B(x, y, \phi) = \sum_{i,j} c_{i,j} B(i, j) \tag{C2}$$

where $B(i, j)$ is the value of B at jth toroidal angle and ith vertice ofthe triangle cell in which the particle is located. The weight coefficients $c_{i,j}$ are determined by particle location (x, y, ϕ). We advance each particle both in the cylindrical coordinates and the (x, y, ϕ) coordinates. The evolution equations for (R, Z, ϕ) follows directly from Eq. (9). The equations in (x, y, ϕ) coordinates can be obtained by using chain rule:

$$\frac{dx}{dt} = \left(\frac{dR}{dt} - \frac{d\phi}{dt}\frac{\partial R}{\partial \phi}\right)\frac{\partial x}{\partial R} + \left(\frac{dZ}{dt} - \frac{d\phi}{dt}\frac{\partial Z}{\partial \phi}\right)\frac{\partial x}{\partial Z}$$
$$\frac{dy}{dt} = \left(\frac{dR}{dt} - \frac{d\phi}{dt}\frac{\partial R}{\partial \phi}\right)\frac{\partial y}{\partial R} + \left(\frac{dZ}{dt} - \frac{d\phi}{dt}\frac{\partial Z}{\partial \phi}\right)\frac{\partial y}{\partial Z} \tag{C3}$$

16

Finally, the perturbed particle pressures can be determined straightforwardly by using Eq. (B8) and the weight coefficients as follows:

$$
\begin{aligned}
\delta P_{\parallel} &= \sum_k M v_{\parallel}^2 (w_k + \frac{\delta B^{\star\star}}{B^{\star\star}}(\frac{f_k}{g_k} - w_k)) c_{i,j}/dV_i \\
\delta P_{\perp} &= \sum_k \frac{1}{2} M v_{\perp}^2 (w + \frac{\delta B^{\star\star}}{B^{\star\star}}(\frac{f}{g} - w) + \frac{\delta B}{B}\frac{f}{g}) c_{i,j}/dV_i
\end{aligned}
\tag{C4}
$$

in the limit of zero-gyroradius. Here subscript k is the particle index and dV_i is the volume associated with the kth particle's triangle cell.

REFERENCES

[1] ITER Physics Basis Editors et al, Nucl. Fusion 39, 2137 (1999).

[2] W. Park, E.V. Belova, G.Y. Fu *et al.*, Phys. Plasmas **6** 1796 (1999).

[3] L.E. Sugiyama and W Park, Phys. Plasmas **7**, 4644 (2000).

[4] G.Y. Fu and W. Park, Phys. Rev. Lett. **74**, 1594 (1995).

[5] G.Y. Fu *et al.*, the 2002 APS division of plasma physics meeting.

[6] G.Y. Fu, J. Breslau, E. Fredrickson *et al.*, 2004 IAEA Fusion Energy conference (Vilamoura, Portugal), paper TH/P4-38.

[7] H.R. Strauss, L.E. Sugiyama, G.Y. Fu *et al.*, Nucl. Fusion **44**, 1008 (2004).

[8] J.W. Van Dam, M.N. Rosenbluth and Y.C. Lee, Phys. Fluids **25**, 1349 (1982)

[9] F. Porcelli, Plas. Phys. Contro. Fusion **33**, 1601 (1991).

[10] R.B. White, L. Chen, F. Romanelli and R. Hay, Phys. Fluids **28**, 278 (1985).

[11] B. Coppi, R.J. Hastie, S. Migliuolo *et al.*, Phys. Lett. **132A**, 267 (1988).

[12] R.O. Dendy, R.J. Hastie, K.G. McClements and T.J. Martin, Phys. Plasmas **2**, 1623 (1995).

[13] K.G. McClements, R.O. Dendy, C.G. Gimblett *et al.*, Nucl. Fusion **35**, 1761 (1995).

[14] C.Z. Cheng, Phys. Reports **211**, 1 (1992).

[15] Y. Wu, C.Z. Cheng, R.B. White, Phys. Plasmas **1**, 3369 (1994).

[16] J.P. Graves, O. Sauter, and N.N. Gorelenkov, Phys. Plasmas **10**, 1034 (2003).

[17] K. McGuire, R. Goldston, M. Bell *et al.*, Phys. Rev. Lett. **50**, 891 (1983).

[18] L. Chen, R.B. White, M.N. Rosenbluth, Phys. Rev. Lett. **52**, 1122 (1984).

[19] B. Coppi and F. Porcelli, Phys. Rev. Lett. **57**, 2272 (1985).

[20] E. Fredrickson, L. Chen, and R. White, Nucl. Fusion **43**, 1258 (2003).

[21] R. Betti, Plas. Physics Contro. Fusion **35**, 941 (1993).

[22] B. Coppi, S. Migliuolo and F. Porcelli, Phys. Fluids **31**, 1630 (1988).

[23] W.W. Heidbrink *et al.*, Phys. Fluids **B5**, 2176 (1993).

[24] J. Candy, H.L. Berk, B.N. Breizman *et al.*, Phys. Plasmas **6**, 1822 (1999).

[25] A. Odblom, B.N. Breizman, S.E. Sharapov *et al.*, Phys. Plasmas **9**, 155 (2001).

[26] S. Briguglio, G. Vlad, F. Zonca, and C. Kar, Phys. Plasmas **2**, 3711 (1995).

[27] Y. Todo and T. Sato, Phys. Plasmas **5**, 1321 (1998).

[28] C.Z. Cheng, Phys. Fluids **B3**, 2463 (1991).

[29] R. Budny, private communication, 2002.

[30] H.L. Berk, B.N. Breizman, and J. Candy *et al.*, Phys. Plasmas **6**, 3102 (1999).
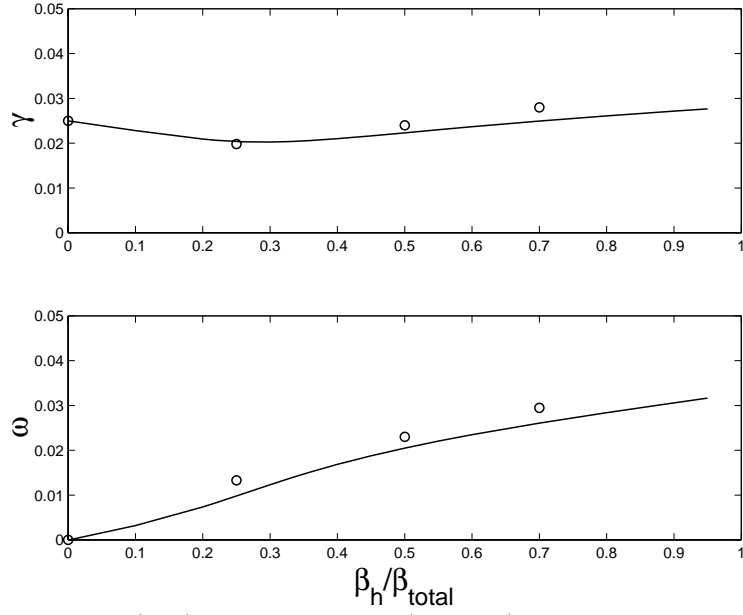
FIG. 1. The growth rate (top) and frequency (bottom) of the $n = 1$ mode as a function of energetic particle beta fraction
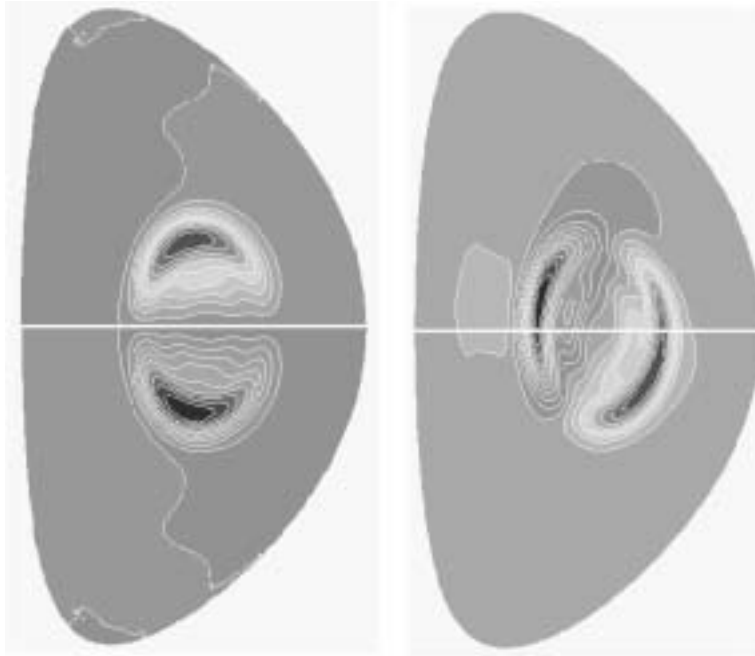
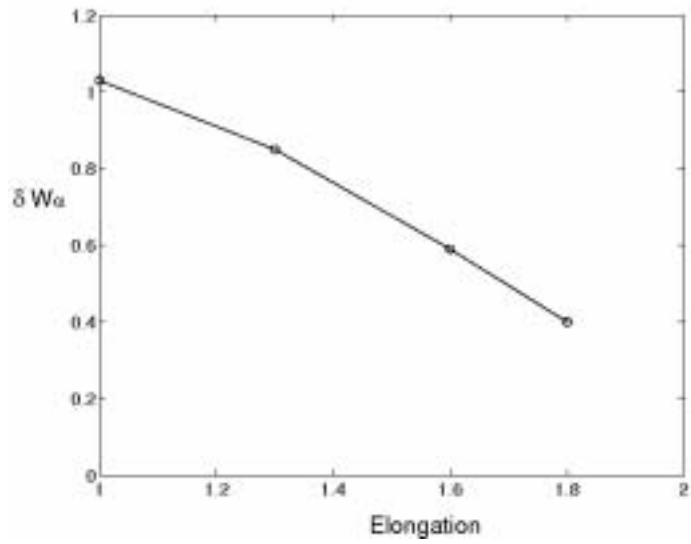FIG. 2. The n=1 internal kink mode structure with (right) and without(left) alpha particles.

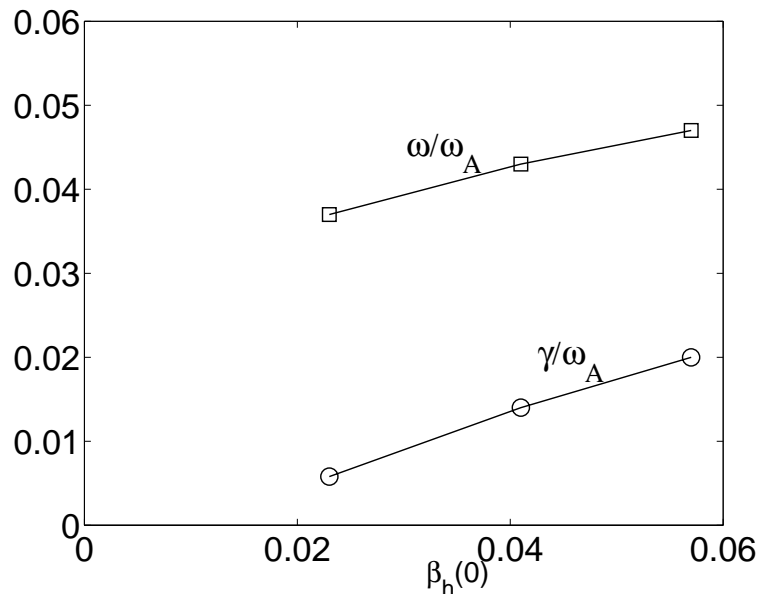FIG. 3. The alpha particle stabilizing contribution δW_α as a function of elongation.

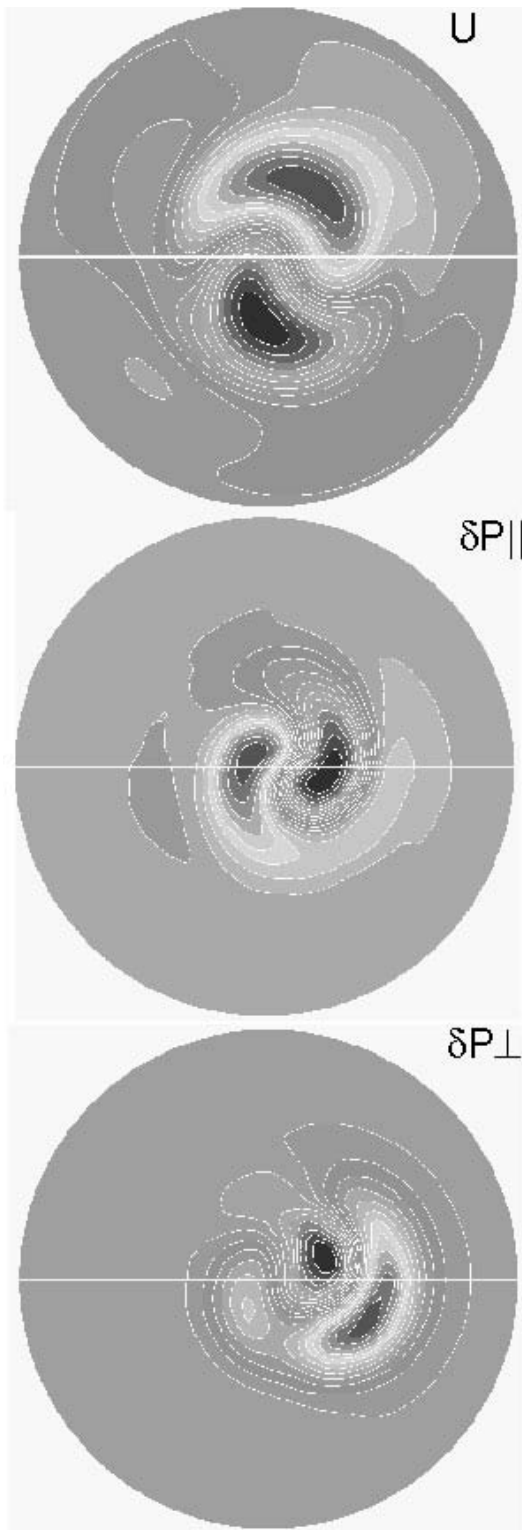FIG. 4. The fishbone mode frequency and growth rate versus energetic particle beta.

FIG. 5. The contours of the fishbone linear eigenmode for velocity stream function U and the perturbed energetic particle pressure $\delta P_\parallel$ and $\delta P_\perp$.
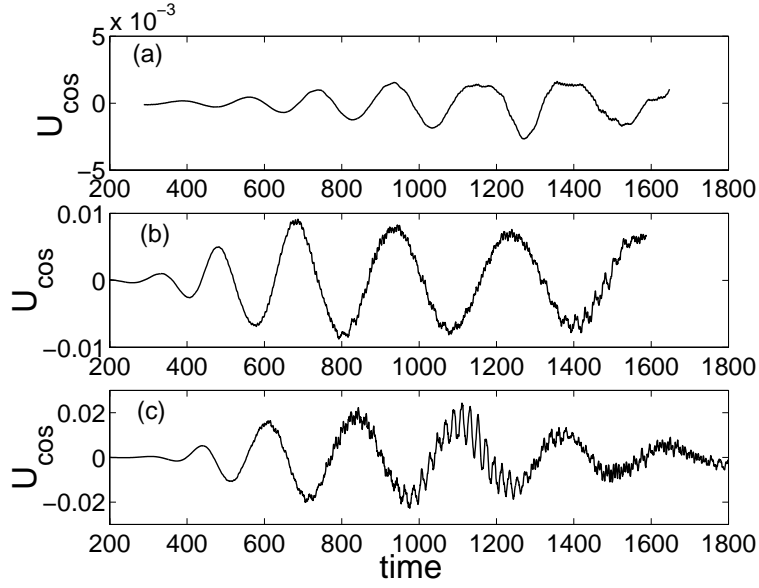
FIG. 6. Nonlinear evolution of the *cos* component of U for case A (upper plot), B (middle plot) and C (lower plot).
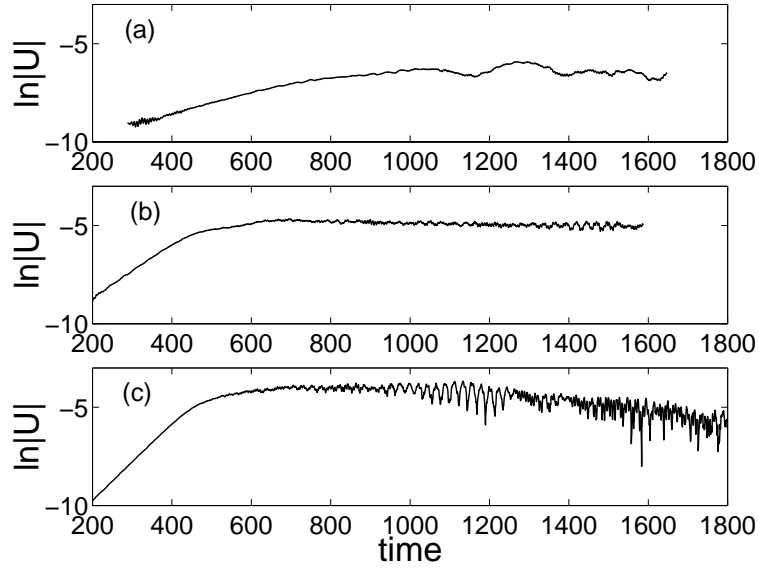

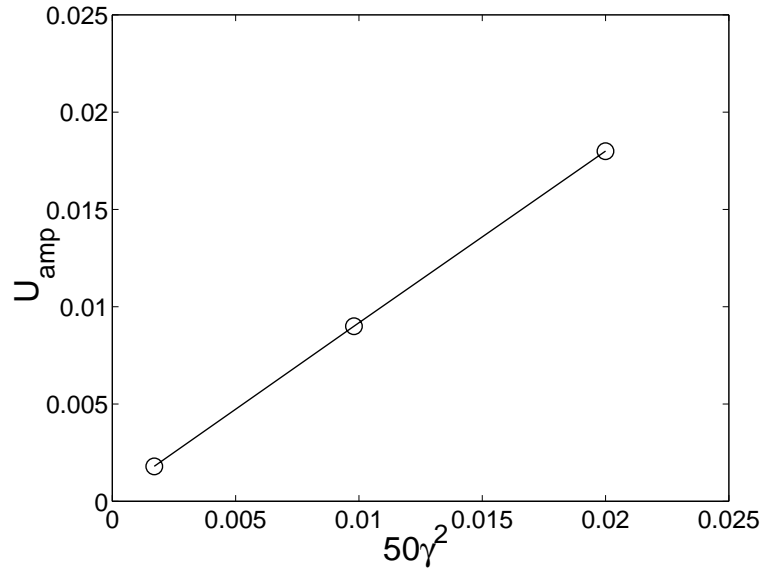FIG. 7. The nonlinear evolution of the mode amplitude $ln|U|$ for case A (upper), B (middle) and C (lower).

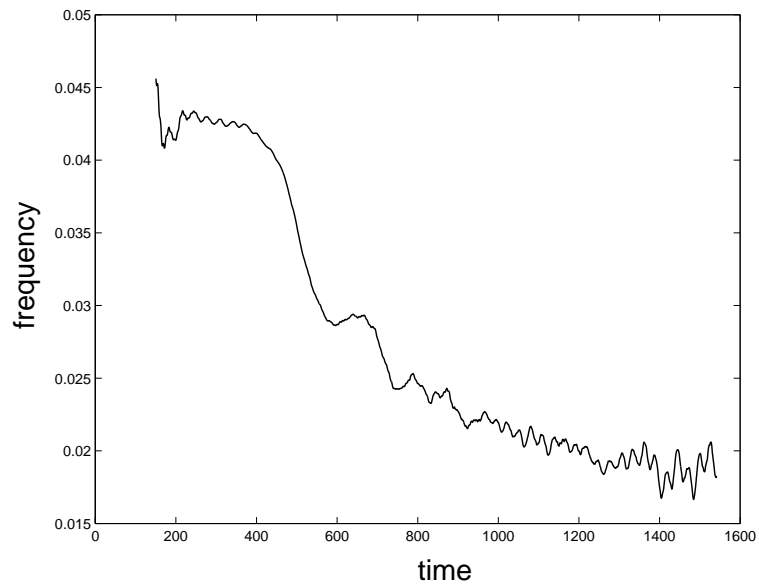FIG. 8. The initial saturation amplitude of U versus $50\gamma^2$.

FIG. 9. The nonlinear evolution of the fishbone mode frequency for case B.
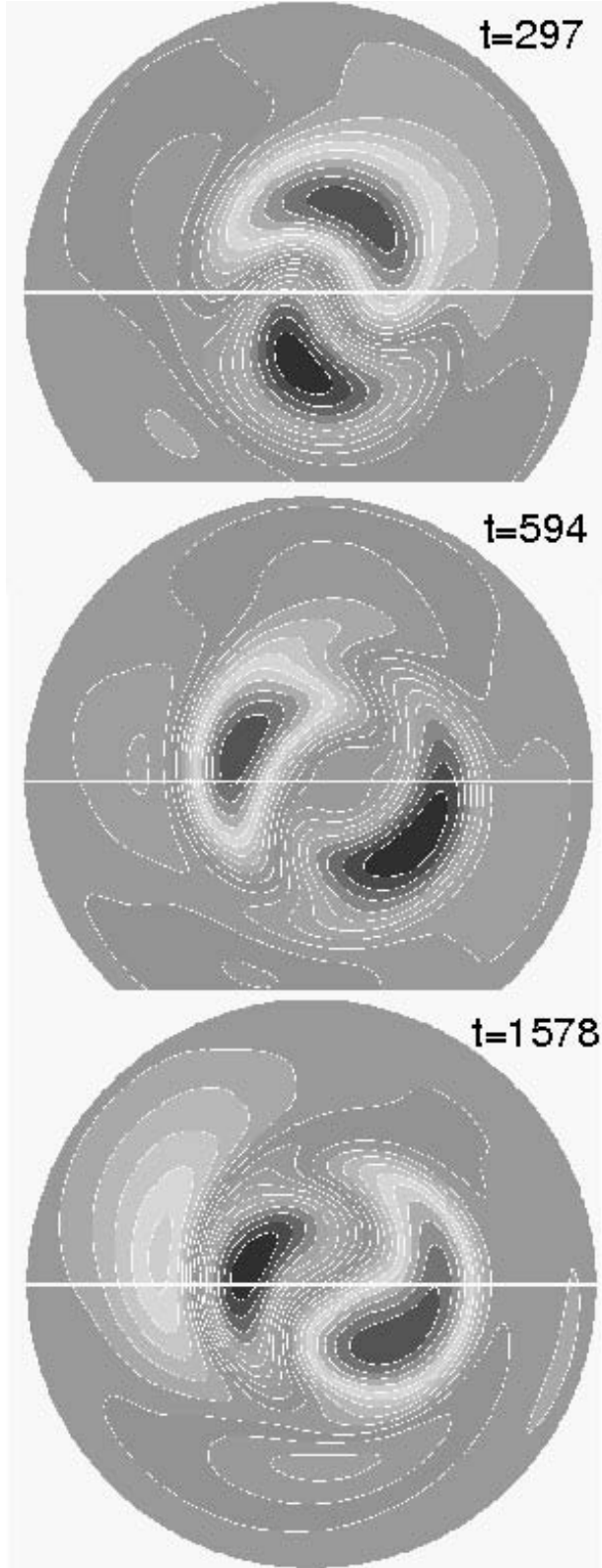
24

FIG. 10. The fishbone mode structure of U for case B at three time slices: (a)in linear stage at $t = 297$, (b)near initial saturation at $t = 594$, and (c)in late nonlinear stage at $t = 1578$.
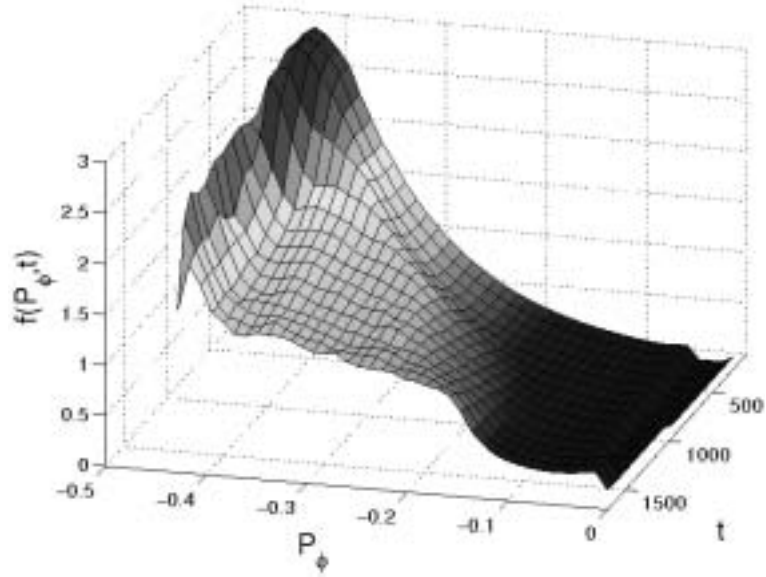
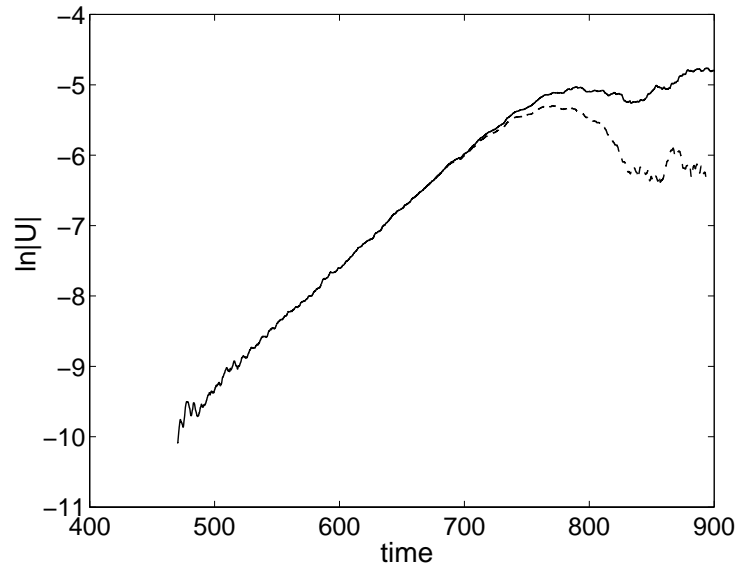FIG. 11. The trapped particle distribution function versus time at $v/v_A = 0.8$ and $\Lambda = 1.0$.

FIG. 12. The evolution of the mode amplitude $ln|U|$ with (dashed line) and without (solid line) fluid nonlinearity.

External Distribution

Plasma Research Laboratory, Australian National University, Australia

Professor I.R. Jones, Flinders University, Australia

Professor João Canalle, Instituto de Fisica DEQ/IF - UERJ, Brazil

Mr. Gerson O. Ludwig, Instituto Nacional de Pesquisas, Brazil

Dr. P.H. Sakanaka, Instituto Fisica, Brazil

The Librarian, Culham Science Center, England

Mrs. S.A. Hutchinson, JET Library, England

Professor M.N. Bussac, Ecole Polytechnique, France

Librarian, Max-Planck-Institut für Plasmaphysik, Germany

Jolan Moldvai, Reports Library, Hungarian Academy of Sciences, Central Research
Institute for Physics, Hungary

Dr. P. Kaw, Institute for Plasma Research, India

Ms. P.J. Pathak, Librarian, Institute for Plasma Research, India

Dr. Pandji Triadyaksa, Fakultas MIPA Universitas Diponegoro, Indonesia

Professor Sami Cuperman, Plasma Physics Group, Tel Aviv University, Israel

Ms. Clelia De Palo, Associazione EURATOM-ENEA, Italy

Dr. G. Grosso, Instituto di Fisica del Plasma, Italy

Librarian, Naka Fusion Research Establishment, JAERI, Japan

Library, Laboratory for Complex Energy Processes, Institute for Advanced Study,
Kyoto University, Japan

Research Information Center, National Institute for Fusion Science, Japan

Professor Toshitaka Idehara, Director, Research Center for Development of Far-Infrared Region,
Fukui University, Japan

Dr. O. Mitarai, Kyushu Tokai University, Japan

Mr. Adefila Olumide, Ilorin, Kwara State, Nigeria

Dr. Jiangang Li, Institute of Plasma Physics, Chinese Academy of Sciences, People's Republic of China

Professor Yuping Huo, School of Physical Science and Technology, People's Republic of China

Library, Academia Sinica, Institute of Plasma Physics, People's Republic of China

Librarian, Institute of Physics, Chinese Academy of Sciences, People's Republic of China

Dr. S. Mirnov, TRINITI, Troitsk, Russian Federation, Russia

Dr. V.S. Strelkov, Kurchatov Institute, Russian Federation, Russia

Kazi Firoz, UPJS, Kosice, Slovakia

Professor Peter Lukac, Katedra Fyziky Plazmy MFF UK, Mlynska dolina F-2, Komenskeho Univerzita,
SK-842 15 Bratislava, Slovakia

Dr. G.S. Lee, Korea Basic Science Institute, South Korea

Dr. Rasulkhozha S. Sharafiddinov, Theoretical Physics Division, Insitute of Nuclear Physics, Uzbekistan

Institute for Plasma Research, University of Maryland, USA

Librarian, Fusion Energy Division, Oak Ridge National Laboratory, USA

Librarian, Institute of Fusion Studies, University of Texas, USA

Librarian, Magnetic Fusion Program, Lawrence Livermore National Laboratory, USA

Library, General Atomics, USA

Plasma Physics Group, Fusion Energy Research Program, University of California at San Diego, USA

Plasma Physics Library, Columbia University, USA

Alkesh Punjabi, Center for Fusion Research and Training, Hampton University, USA

Dr. W.M. Stacey, Fusion Research Center, Georgia Institute of Technology, USA

Director, Research Division, OFES, Washington, D.C. 20585-1290

05/16/05

The Princeton Plasma Physics Laboratory is operated
by Princeton University under contract
with the U.S. Department of Energy.

Information Services
Princeton Plasma Physics Laboratory
P.O. Box 451
Princeton, NJ 08543

Phone: 609-243-2750
Fax: 609-243-2751
e-mail: pppl_info@pppl.gov
Internet Address: http://www.pppl.gov